Hindawi
Mathematical Problems in Engineering
Volume 2018, Article ID 1619297, 13 pages
https://doi.org/10.1155/2018/1619297

Research Article

Assessment of Bearing Dynamic Characteristics by Numerical Modeling with Effects of Oil Film and Centrifugal Deformation

Jie Yu,[1,2] Wei Yuan,[2] Songsheng Li ,[1] and Wenbing Yao[3]

[1]*Shanghai Key Laboratory of Mechanical Automation and Robotics, Shanghai University, Shanghai 200072, China*
[2]*School of Mechanical Engineering, Shandong University of Technology, Zibo 255049, China*
[3]*Jude Construction and Installation Co., Ltd., Zibo, Shandong 255000, China*

Correspondence should be addressed to Songsheng Li; 03810020@shu.edu.cn

Received 24 April 2018; Revised 30 August 2018; Accepted 22 October 2018; Published 6 November 2018

Academic Editor: Anders Eriksson

This paper developed a modified quasi-static model (MQSM), considering the oil film thickness between the bearing parts and the centrifugal deformation of the inner ring, and contrasting with traditional quasi-static model (TQSM), to analyze the dynamic characteristics of spindle bearing. The model was verified with the experimental results. A systematic parametric analysis was made to investigate the influence of applied load, inner ring rotation speed (ni), and the radius coefficient of groove curvature (RCR) on the contact load, contact angle, and heat generating rate. The results show that there is a smaller influence on the contact load, contact angle, and heat generation of bearing with the changes of ni and axial load (F_a) of bearing in the case of MQSM and TQSM. But the radial load (F_r) and RCR have great influence on this.

1. Introduction

Kinematic accuracy of the main shafts commonly determines the machining quality, performance, service life, and reliability of high-speed machine tool, in which the supporting spindle bearings play a very important role [1, 2]. The higher speed and reliability of spindle bearings subjected to the continuously large thrust loading are demanded during high rotational speed machining. Therefore, it is necessary to create an accurate model to reflect the dynamic characteristics of spindle bearings, including rotational speed, contact temperature, and dynamic loading [3–6]. Especially, the oil film thickness and inner ring centrifugal deformation should be taken into account for the assessments of the spindle bearings' dynamic characteristics, which may significantly affect the geometry relationship of the bearing internal channel curvature center and the ball center obviously.

It was found that the centrifugal expansion deformation of the bearing inner ring is much larger than the deformation of the shaft with the increase of rotational speed. Based on a dynamic model of spindle bearings, the research of Cao et al. [7] indicated that the bearing contact angle decreases with the increase of contact load by introducing the centrifugal expansion deformation of the bearing inner ring. The general spindle bearing FEM [8] showed that the impact factors of high-speed system, such as bearing radial stiffness, centrifugal force, and gyroscopic moments, have a significant effect on dynamic characteristics of spindle system in high speeds. A coupled spindle bearing model was established considering the centrifugal deformation by Hong et al. [9], and the simulation and experimental results indicated that there is a correlation between the natural frequency and the number of bearings. The Jones' bearing model was updated by Guo et al. [10], by considering of radial centrifugal expansion and thermal deformations on the geometric displacement in the bearings, which can predict the contact angle, deformation, and load between rolling elements and bearing raceways more accurately.

During the high rotating process of the spindle bearings, lubrication oil film can also bear a part of multiple orientation loading, which plays significantly important roles in the dynamic characteristics and the distance between the bearing internal channel curvature center and the ball center [11–14]. The shear of oil film will cause remarkable heat of hydrostatic hydrodynamic hybrid bearings, which will lead to decreasing of bearing clearance and even seizure especially at high rotational speed [15]. An integrated thermal model [16] was numerically established to calculate the heat generation of spindle bearings and temperature distribution of the spindle system, considering the rotation speed, preload, and oil film thickness. Therefore, the machine performance and dynamic design of machine spindle can be improved by taking into account the impact of oil film thickness.

To analyze the bearing dynamic characteristics, the typical quasi-statics modeling of spindle bearings was widely utilized. A five degrees of freedom quasi-static model of ball bearing under nonuniform preload was established by Li et al. [17], and the results indicated that proper nonuniform preload can improve the contact status between balls and rings and can also reduce the heat generation rate and the excessive local heat in ball bearing under practical working conditions. Kim et al. [18] employed the quasi-static analysis model by taking dynamic effects into account to optimize the nonstandard angular contact ball bearing for the main shaft of a grinder. The fatigue life calculations in rolling bearing simulations were evaluated by a new quasi-static multidegree of freedom tapered roller bearing model by considering non-Hertz contact pressures in time-domain simulations [19]. However, the assessment of the dynamic characteristics of the contact load, contact angle, and bearing heat with the increase of rotational speed, axial load, radial load, and coefficient of raceway curvature radius (RCR) had not taken into account both the factors of film oil thickness and centrifugal deformation. Therefore, the establishment of considering both the deformation of film thickness and centrifugal bearing mechanics model is extraordinarily important for a more accurate analysis of the dynamic characteristics of the spindle bearings.

In this paper, a modified quasi-statics model (MQSM) was established by considering the influence of film thickness and centrifugal deformation, which is expected to make the bearing dynamic performance analysis more effective. Section 2 showed the calculation algorithms of the deformation of inner rings and rotors with the effect of film thickness and centrifugal expansion deformation. The MQSM was established in Section 3 by considering film thickness and centrifugal expansion deformation to reflect spindle bearings' dynamic characteristics. The spindle bearing heat was applied as the comparison parameter with the experimental results, the calculation of which was shown in Section 4. The experimental and MQSM results in Section 5 were given and discussed, to reveal the changing rule of the dynamic characteristic parameters of the spindle bearings. Section 6 presented the concluding remarks.

2. Deformation of Inner Ring and Rotor

2.1. Introducing Centrifugal Expansion Deformation. The centrifugal force of bearing inner rings can hardly be ignored and will result in centrifugal expansion deformation, particularly in high rotational speed. On the basis of the elastic mechanics theory, the bearing inner rings and the cooperating rotating shafts are simplified in advance as the thin-walled rings and the thick walled cylinder, respectively. Thereafter, centrifugal expansion deformation calculation formula can be deduced at the coordination position of the shaft and the inner ring by (1) and (2) [7]:

$$u_{cs} = \frac{\rho_s \omega_i^2}{16E_s}\left[\left(3+\nu_s\right)d_s^2 + \left(1-\nu_s\right)d^3\right]d \tag{1}$$

$$u_{ci} = \frac{\rho_i \omega_i^2}{16E_i}\left[\left(3+\nu_i\right)d^2 + \left(1-\nu_i\right)d_i^2\right]d_i \tag{2}$$

where u_{cs} is the centrifugal expansion deformation of shafts; ρ_s, ν_s, and E_s are the density, poison ratio, and elasticity modulus of the shaft, respectively; d_s is the inner diameter of the spindle; u_{ci} is the centrifugal expansion deformation of the inner ring; ρ_i, ν_i, and E_i are the density, poison ratio, and elasticity modulus of inner ring, respectively; ω_i is the angular speed of inner ring; d and d_i are the inner diameters of the inner ring and its channel, respectively.

The mutual interference fit coupling and constraints among the inner ring and shaft have frequently occurred, whereas the centrifugal expansion of the inner ring diameter and rotor outer diameter can reduce the amount of interference on fit surfaces, when subjected to centrifugal force. The magnitude of interference caused by centrifugal expansion of the shaft and the inner ring can thus be determined as

$$I_c = u_{ci} - u_{cs} \tag{3}$$

As known, centrifugal force deformation is proportional to the square of the rotating speed, and the centrifugal force deformation mainly occurred on the inner ring on the mating surfaces of the shaft and the inner ring with the rotational speed increase. The shaft centrifugal expansion deformation has less effect on the change of bearing radial internal clearance. Thereby, the factor of the centrifugal expansion deformation of the inner rings will be merely taken into account to research the impact of the centrifugal expansion deformation of the inner rings and shafts on the bearing internal geometry relationship.

2.2. Introducing Oil Film Thickness. Lubrication condition plays remarkable role in spindle bearings; therefore, certain thickness of oil film between ring channels should be recommended. Based on the theory of elastic hydrodynamic lubrication (EHL), oil film stiffness is determined by the minimum oil film thickness. Under the condition of isothermal and adequate oil supply, dimensionless center oil film thickness H_o and dimensionless minimum oil film thickness H_{min} between rolling body and ring channel can be determined as [11]

$$\begin{aligned} H_0 &= 2.69U^{0.67}G^{0.53}W^{-0.067}\left(1-0.61e^{-0.73k}\right) \\ H_{\min} &= 3.63U^{0.68}G^{0.49}W^{-0.073}\left(1-e^{-0.68k}\right) \end{aligned} \tag{4}$$

where U is the dimensionless velocity parameters; G is the dimensionless material parameters; W is the dimensionless load parameters; k is the ellipticity. Thereafter, center oil film thickness h_0 and minimum oil film thickness H_{min} between the rolling body and ring channel are then determined as

$$\begin{aligned} h_0 &= R_x H_0 \\ &= 2.69U^{0.67}G^{0.53}W^{-0.067}\left(1-0.61e^{-0.73k}\right)R_x \\ h_{\min} &= R_x H_{\min} \\ &= 3.63U^{0.68}G^{0.49}W^{-0.073}\left(1-e^{-0.68k}\right)R_x \end{aligned} \quad (5)$$

where R_x is the rolling element along the movement direction of the equivalent radius of curvature.

Figure 1 shows the distribution of film thickness and pressure under EHL and nonlinear Hertz contact condition, where the difference is whether considering the existence of lubricating oil film. The existence of the lubricating oil film will reduce the elastic deformation between the roller and the ring channel. Consequently, to calculate the actual contact stiffness, the amount of the radial tendency can be regarded as the radial elastic deformation between the roller and ring channel by considering the oil film thickness, as follows:

$$\Delta\delta = \delta - h_0 \quad (6)$$

where $\Delta\delta$ is the elastic deformation under EHL condition; δ is the elastic deformation at Hertz contact position; h_0 is the central oil film thickness at EHL contact position.

3. The Spindle Bearing Mechanical Characteristics Analysis

3.1. The Ball Motion Analysis. For easy analysis, coordinate system of spindle bearing is established as shown in Figure 2. The parameters ω_{xj}, ω_{yj}, and ω_{zj} are the rotation angular velocity corresponding to the ball 3-D coordinate components of x, y, and z, respectively. The parameters β and β' are the ball's spiral angle and yaw angle, respectively. Assuming $\beta' = 0$ in this paper, the rotation angular velocity in the coordinate component of y will be $\omega_{yj} = 0$.

The outer ring of spindle bearing is set as the fixed part, and constant angular velocity of inner ring rotates is denoted by ω_j. Consequently, the angular velocity of the ball ω_{yj} can be determined as [3]

$$\omega_{mj} = \frac{1-\gamma'\cos\alpha_{ij}}{1+\cos\left(\alpha_{ij}-\alpha_{ej}\right)}\omega_i \quad (7)$$

where $\gamma' = D_b/d_m$, D_b is the ball diameter, d_m is the pitch diameter of the bearing, and α_{ij} and α_{ej} are the contact angles between the ball and the inner and outer ring, respectively.

The ball's rotation angular velocity ω_{bj} is then calculated by [3]

$$\omega_{bj} = \frac{-1}{\left(\left(\cos\alpha_{ej}+tg\beta_j\sin\alpha_{ej}\right)/\left(1+\gamma'\cos\alpha_{ej}\right)+\left(\cos\alpha_{ij}+tg\beta_j\sin\alpha_{ij}\right)/\left(1+\gamma'\cos\alpha_{ij}\right)\right)}\omega_i \quad (8)$$

Given that the spindle bearings are a kind of high-speed bearings, on the basis of the control theory of ring and assuming the outer raceway is controlled, the spiral angle β_i can be determined as

$$tg\beta_j = \frac{\sin\alpha_{ij}}{\cos\alpha_{ij}-\gamma'} \quad (9)$$

Then the spin angular velocity of bearing inner ring can be calculated by

$$\begin{aligned} &\omega_{sj} \\ &= \left(\frac{\omega_{bj}}{\omega}\sin\beta_j\cos\alpha_{ij} - \frac{\omega_{bj}}{\omega}\cos\beta_j\sin\alpha_{ij} + \sin\alpha_{ij}\right)\omega \end{aligned} \quad (10)$$

3.2. Displacement Coordinate Equation. The outer ring and bearing seat are fixed in advance; therefore, the outer ring curvature center will be always in the same position. In our dynamic characteristics analysis model, the relative radial, axial, and angular displacements of bearing inner and outer rings are denoted as δ_a, δ_r, and θ, respectively, caused by the combined action of the radial force F_r, axial force F_a, and moment M. Meanwhile, the geometric positions of the bearing components with the effect of F_r, F_a, and M are shown in Figure 3, in which (i) the axial and radial distances between the inner and outer channel curvature centers are denoted as A_{aj} and A_{rj}, respectively, (ii) the distances between the ball center and the inner and outer channel curvature centers are denoted as L_{ij} and L_{ej}, respectively, and (iii) the axial and radial changed distances of the center of channel curvature are denoted as U_{aj} and V_{rj}, respectively. $\mathrm{U_{aj}}$, $\mathrm{U_{rj}}$

Figure 3 shows the geometric position relationship between the jth ball centers with angle position and the inner and outer channel curvature centers.

Without the effect of loading, the distance between the inner and outer channel curvature centers can be determined as

$$\overline{AB} = \left(f_i + f_e - 1\right)D_b' \quad (11)$$

where f_i and f_e are the inner and outer raceway groove curvature radius ratios, respectively. D_b' is the ball diameter after considering deformation.

The ball locations of the jth ball are obtained by

$$\begin{aligned} A_{aj} &= \overline{AB}\sin\alpha_0 + U_{aj} \\ A_{rj} &= \overline{AB}\cos\alpha_0 + V_{rj} \end{aligned} \quad (12)$$

where α_0 is the initial contact angle.

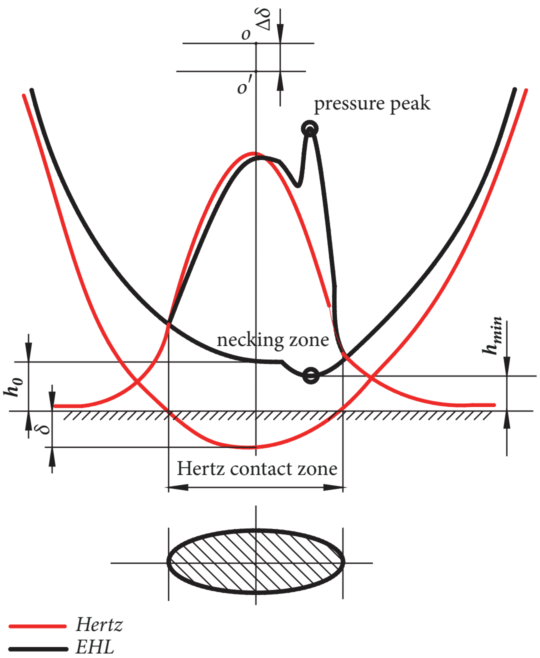

FIGURE 1: The distribution of film thickness and pressure under EHL and Hertz contact condition.

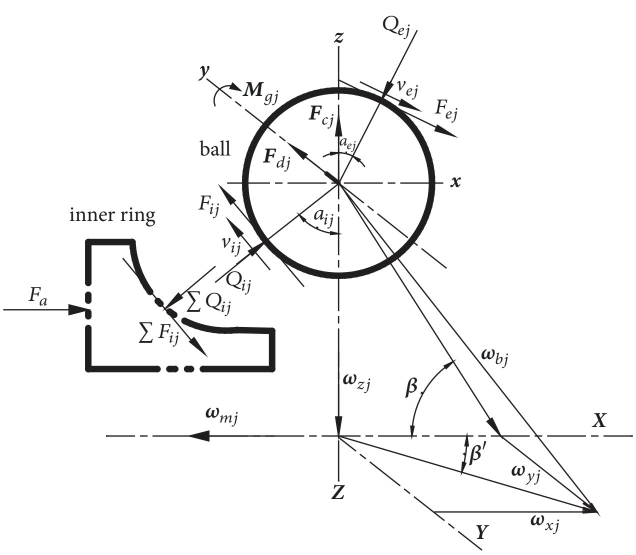

FIGURE 2: Movement and force of the inner ring and ball in the bearing coordinate system.

As shown in Figure 3, according to the relative position of curvature center, the displacement coordinate equations of the ball center change:

$$\begin{aligned} L_{ij}\sin\alpha_{ij} + L_{ej}\sin\alpha_{ej} - A_{aj} &= 0 \\ L_{ij}\cos\alpha_{ij} + L_{ej}\cos\alpha_{ej} - A_{rj} &= 0 \end{aligned} \tag{13}$$

Assessments of the spindle bearings' dynamic characteristics by traditional quasi-statics model (TQSM) used to pay no attention to the effect of the oil film thickness and

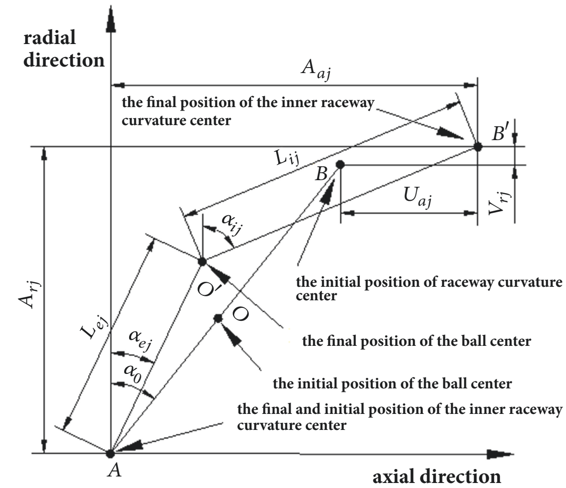

FIGURE 3: The position relationship between the jth ball center and the inner and outer channel curvature centers.

centrifugal force, which will affect the geometry relationship of the bearing internal channel curvature center and the ball center obviously. In this paper, to make the bearing dynamic performance analysis more accurate, a modified quasi-statics model (MQSM) was established by considering the influence of film thickness and centrifugal deformation. Therefore, the modified parameters of U_{aj}, V_{rj}, L_{ij}, and L_{ej}, as shown in Figure 3, are redefined considering the oil film thickness as follows:

$$\begin{aligned} U_{aj} &= \delta_a + \theta R_i \cos\varphi_j \\ V_{rj} &= \delta_r \cos\varphi_j + u_{ci} \\ L_{ij} &= \left(f_i - 0.5\right) D_b + \delta_{ij} - h_{ij} \\ L_{ej} &= \left(f_e - 0.5\right) D_b + \delta_{ej} - h_{ej} \end{aligned} \tag{14}$$

where R_i is the circular radius of inner ring channel curvature center, u_{ci} is the inner ring centrifugal force deformation, δ_{ij} and δ_{ej} are the Hertz elastic deformations at the jth ball and the inner and outer contact points, respectively, and h_{ij} and h_{ej} are the center oil film thickness at the jth ball and inner and outer ring contact point, respectively.

3.3. Force Balance Equation of Ball and Inner Ring. When the bearing is at high speed, the ball and the inner ring stresses can be shown as in Figure 2. Force equilibrium equations of each ball can be established as follows:

$$\begin{aligned} &Q_{ij}\sin\alpha_{ij} - Q_{ej}\sin\alpha_{ej} + F_{ij}\cos\alpha_{ij} - F_{ej}\cos\alpha_{ej} = 0 \\ &Q_{ij}\cos\alpha_{ij} - Q_{ej}\cos\alpha_{ej} - F_{ij}\sin\alpha_{ij} + F_{ej}\sin\alpha_{ej} + F_{cj} \\ &\quad = 0 \end{aligned} \tag{15}$$

where K_{ij} and K_{ej} are the contact stiffness coefficients between ball and inner and outer rings, respectively; F_{cj} is the centrifugal force of the jth ball; F_{ij} and F_{ej} are the friction force between the ball and inner and outer rings, respectively.

The force balance equations of the inner ring in the horizontal and vertical direction, and moment equilibrium conditions can be written as

$$\begin{aligned} & F_a - \sum_{j=1}^{Z} \left(Q_{ij} \sin \alpha_{ij} + F_{ij} \cos \alpha_{ij} \right) = 0 \\ & F_r - \sum_{j=1}^{Z} \left(Q_{ij} \cos \alpha_{ij} - F_{ij} \sin \alpha_{ij} \right) \cos \psi_j = 0 \\ & M - \sum_{j=1}^{Z} \left[\left(Q_{ij} \sin \alpha_{ij} + F_{ij} \cos \alpha_{ij} \right) R_i - r_i F_{ij} \right] \cos \psi_j \\ & \quad = 0 \end{aligned} \tag{16}$$

where R_i is the curvature radius of the inner ring channel.

4. The Spindle Bearing Heat

Based on the calculation theory of Harris high-speed bearing frictional heat, the generated heat of the spindle bearing mainly includes the following several parts.

(1) Power loss of the mating pairs of ball and raceway during relative sliding process can be determined as

$$H_{rj} = F_{rj} v_{rj} \quad r = i, e \tag{17}$$

where F_{rj} is traction force between the jth ball and its ring in the direction of the ellipse long axis and v_{rj} is relative sliding velocity between the jth ball and its ring in the direction of the ellipse long axis.

(2) Spin movement between the ball with the inside and outside raceway is an important factor to the power loss [6]

$$\begin{aligned} M_{sj} &= \frac{3\mu Q_j a_j \Sigma_j}{8} \\ H_{sj} &= M_{sj} \omega_{sj} \end{aligned} \tag{18}$$

where M_{sj} is the jth ball spin torque, μ is the friction coefficient, Q_j is the contact load between the jth ball and its ring, Σ_j is the complete elliptic integral of the second kind between the jth ball and its ring, α_j is the contact ellipse semimajor axis, and ω_{sj} is the spin angular velocity of the jth ball.

(3) Because of power loss caused by the gyroscopic motion, the jth ball can be determined as

$$\begin{aligned} M_{gj} &= J \omega_{mj} \omega_{oj} \sin \beta_j \\ H_{gj} &= M_{gj} \omega_{yj} \end{aligned} \tag{19}$$

where M_{gj} is the gyroscopic moment of the jth ball, J is the inertia moment, ω_{mj} is the orbital angular velocity of the jth ball, and ω_{bj} is the rotation angular velocity of the jth ball.

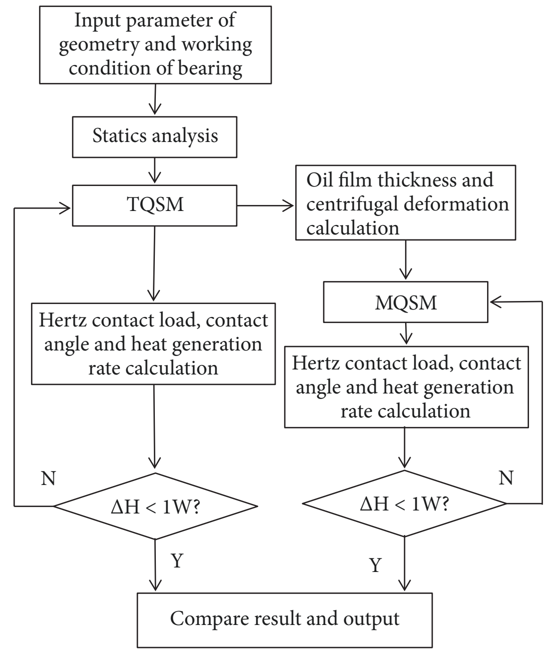

Figure 4: Flow chart of the MQSM establishment.

(4) With the ball revolution, the power loss caused by viscous damping effect of the mixture of oil and gas can be determined as

$$\begin{aligned} F_{dj} &= \frac{\rho_{oa} \pi C_D D_b^2 \left(d_m \omega_{mj} \right)}{320} \\ H_{dj} &= \frac{F_{dj} \omega_{mj} d_m}{2} \end{aligned} \tag{20}$$

where F_{dj} is the resistance force of the jth ball caused by the mixture of oil and gas, ρ_{oa} is the density of the mixture of oil and gas, and C_D is the resistance coefficient.

Finally, the total power loss of the bearing can be determined as

$$H_{total} = \sum_{j=1}^{z} \left(H_{brj} + H_{sj} + H_{gyj} + H_{dj} \right) + H_{co} \tag{21}$$

where z is the number of the ball.

5. The MQSM Model Results and Discussion

5.1. Experimental Assessment. The MQSM of the spindle bearing was established by MATLAB tool, and the flow chart is shown in Figure 4. To evaluate the MQSM availability, experiments were conducted on a self-designed motorized spindle bearing rig (Figure 5) in Shanghai Intelligent Manufacturing and Robot Key Laboratory. The required equipment and test instruments include test spindle (model 80GS60A), electric spindle support, a pair of B7006C bearing, motorized spindle overhang shaft, bearing inner and outer baffle, sleeve, compressive bar, waveform, Jordan weight, piezoelectric pressure sensor, temperature sensor and related Labview

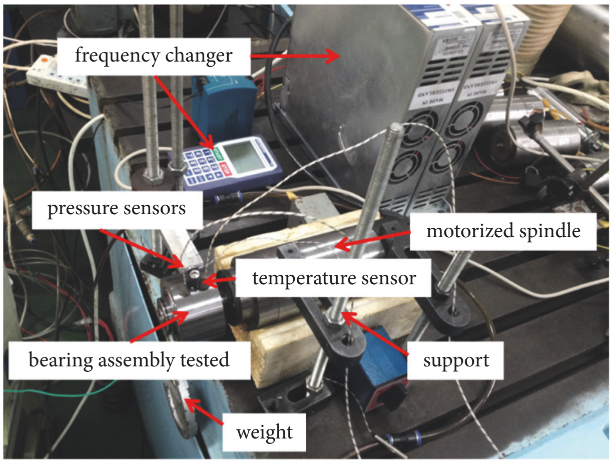

FIGURE 5: The self-designed motorized spindle bearing rig.

signal acquisition device, and KOLLMORGEN transducer (model: ACO5000D), as shown in Figure 5.

The test principle is shown in Figure 6. The tested bearings installed back-to-back are installed on the outer end of the rotor of the driving electric spindle, which makes the bearings under test suspended. The driving electric spindle drives the inner ring of the bearings rotating. Because of the friction between the bearing inner and outer ring and balls, the bearing overhanging outer ring and the outer sleeve with its interference fit tend to rotate together with the inner ring without additional resistance. A pressure lever is installed on the sleeve that is fitted with the bearing outer ring, so that the upper end of the sleeve is attached to the piezoelectric pressure sensor fixed on the support. When the outer sleeve rotates with the inner ring, the pressure sensor will be pressed and the pressure F_l will be measured.

The voltage signal measured by the piezoelectric pressure sensor is inputted into the computer through the acquisition card and analyzed and processed by Labview. The value of the friction moment of a single bearing and the actual friction moment of the bearing can be obtained:

$$M_f = \frac{F_l L_l}{2} \tag{22}$$

where M_f is friction moment of the bearing, F_l is the pressure value measured, and L_l is the pressure test point with a distance of 55 mm from the axle center.

$$H_f = M_f \omega_i \tag{23}$$

where H_f is the heat generation power of a single bearing and ω_i is angular velocity of bearing inner ring.

In the test, the change of electric spindle speed is adjusted by frequency changer, and the height difference of inner and outer ring spacer is controlled by waveform ring, so as to adjust the size of bearing axial load. The magnitude of the radial load is changed by lifting the weight on the bolt directly below the bearing outer sleeve.

In the tests, the bearing heat production rates were obtained by the monitored bearing friction torque. Compared with the MQSM results, (i) the experimental results of the bearing heat production rate with various rotation speeds under the conditions of the axial load F_a = 130 N and radial load F_r = 0 N were shown in Figure 7; (ii) the experimental results of the bearing heat production rate with various axial loads under the conditions of inner ring speed n_i = 5000 r/min and radial load F_r = 0N were shown in Figure 8; (iii) the experimental results of the bearing heat production rate with various radial loads under the conditions of inner ring speed n_i = 20000 r/min, axial load F_a = 130 N, were shown in Figure 9.

The results indicate that the change of bearing heat production rates with the increase of rotational speed and axial load, and radial load has similar tendency in experiments and MQSM. Therefore, it can be concluded that the high-speed angular contact ball bearing mechanics model of MQSM in this paper has excellent performance.

5.2. Results of Dynamic Characteristics. The changes of F_a, F_r, *ni,* and RCR have significant influence on the dynamic characteristics of bearing. Based on the variation of these four conditions (Table 1), the variation rule of bearing dynamic parameters is analyzed.

The results of bearing dynamic characteristics in TQSM and MQSM are compared in Figures 10–25. The parameters in this mathematical model of bearing are in ADOSE of P.K. Gupta bearing dynamics program [10] was tabulated in Table 2. The 10 spindle oil was chosen with the lubrication oil dynamic viscosity of η_0=0.027 Pa•s and viscosity coefficient α=2.3e-8Pa^{-1} [11]. The environment temperature of 25°C was set. Ring and ball materials are bearing steel.

During the calculation process, it is found that the bearing sizes are very small comparing the whole bearing system, and the small centrifugal deformation has then little influence on the bearing dynamic characteristics. Therefore, the effect of the centrifugal deformation on the dynamic characteristics can be ignored, and then MQSM just considers the influence of oil film thickness.

5.2.1. Influence of Working Condition and RCR on Oil Film Thickness. F_a, F_r *ni* and RCR have significant influence on the oil film thickness between the bearing inner and outer ring and the ball. The changes of oil film thickness were analyzed in four cases listed in Table 1.

Figures 10 and 11 show the relation curve between the bearing inner and outer rings and the ball with the bearing speed. The figures show that the oil film thickness increases obviously with the increase of *ni*. The oil film thickness between the outer ring and the ball is larger than that of the inner ring.

Figures 12 and 13 show the relation curve of F_a between bearing inner and outer ring and ball. As shown in the figures, as F_a increases, oil film thickness decreases. The reason for this phenomenon is that the increase of F_a reduces the axial clearance inside the bearing.

Figures 14 and 15 show the relation curve of F_r between bearing inner and outer rings and ball. As shown in the figure, with the increase of F_r, the oil film thickness between the bearing inner and outer ring and the ball decreases with

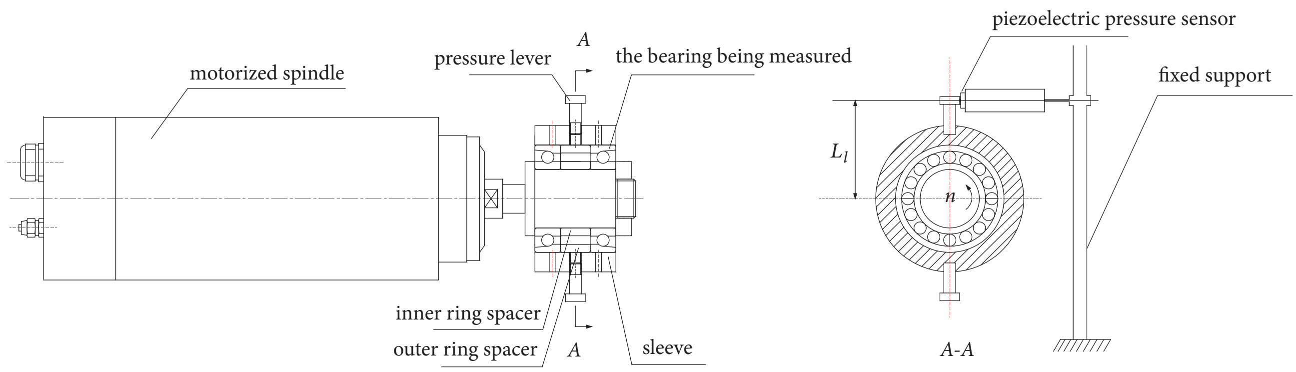

Figure 6: Configuration of the bearing test system.

Table 1: Four different conditions.

operating condition	constant operating condition
F_a=1500:500:3500 N	F_r=100N ni=30000r/min
F_r=1000:500:3000N	F_a=3000N ni=30000r/min
ni=15000:500:35000r/min	F_a=3000N F_r=100N
RCR=0.52:0.01:0.55	F_a=3000N F_i=100N ni =30000r/min

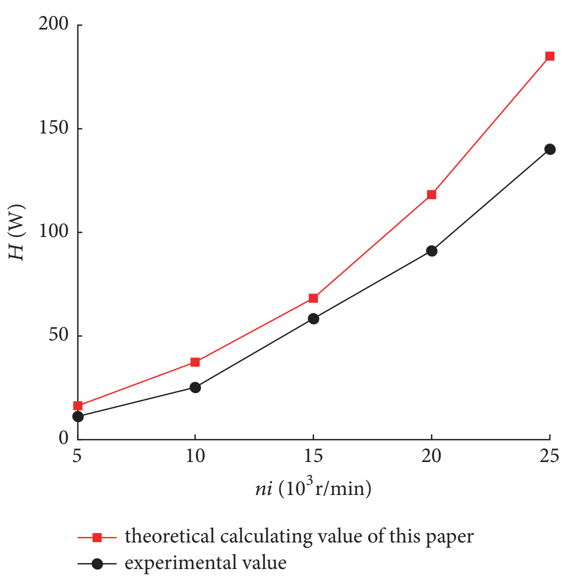

Figure 7: Results of the bearing heat production rate with various rotation speeds.

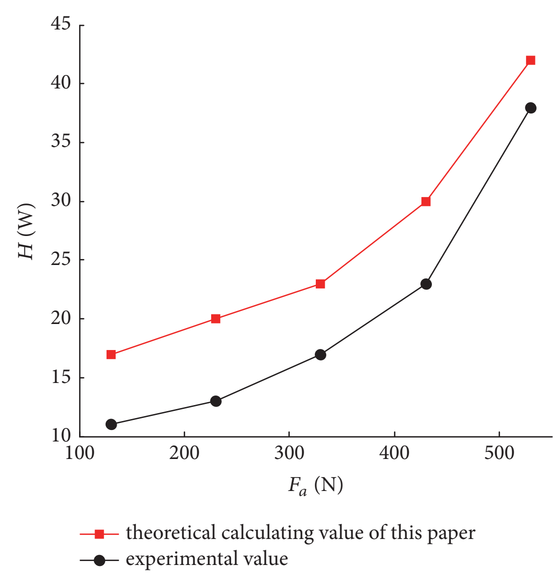

Figure 8: Results of the bearing heat production rate with various axial loads.

the increase of F_r in the loading area. In the nonloaded area, it increased with the increase of F_r. The reason for this phenomenon is that the increase of F_r compacts the ring and ball at the bearing loading area and reduces the radial clearance. In the nonloaded area, the ring and the ball are relaxed and the radial clearance increases.

Figures 16 and 17 show the variation curve of RCR between the bearing inner and outer ring and the ball. As shown in the figure, oil film thickness increases with the increase of RCR. The reason for this phenomenon is that the increase of RCR reduces curvature tolerance between the ring and the ball, which is conducive to the production of oil film. However, if RCR is too large, bearing capacity of bearing will be reduced.

5.2.2. Influence of Working Condition on Dynamic Parameters. Figures 18–20 indicate that with the axial load of 3000 N, the dynamic characteristics of the contact load and bearing heat in TQSM and MQSM have little difference with the increase of the spindle speed from 15000 r/min to 35000 r/min. However, the contact angle of inner rings in MQSM is slightly less than that in TQSM as shown in Figure 10. Meanwhile, with the spindle speed of 30000 r/min, the similar results of

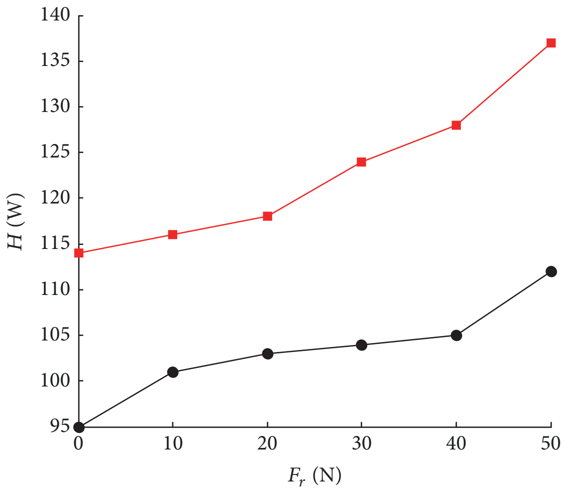

Figure 9: Results of the bearing heat production rate with various radial load.

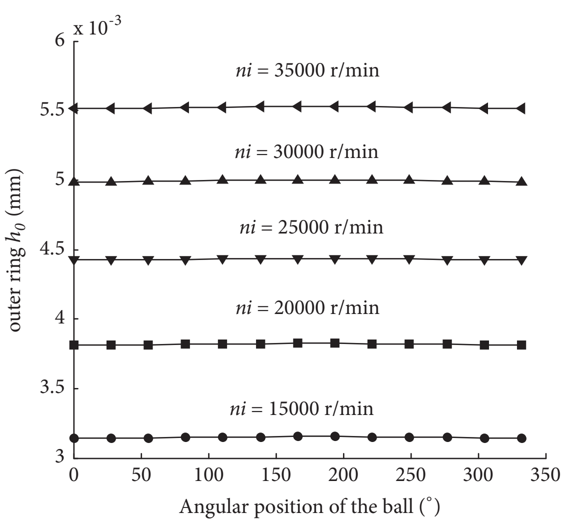

Figure 10: The influence of *ni* on oil film thickness between ball and outer ring.

Table 2: The bearing parameters in MQSM.

Bearing parameters	value
No. of balls	13
Ball diameter (mm)	12
Ball material	GCr15 bearing steel
Contact angle (deg)	15
Inner diameter (mm)	57
Outer diameter (mm)	103
Width (mm)	30
RCR	0.53

the dynamic characteristics with various axial loads can also be illustrated in Figures 21–23.

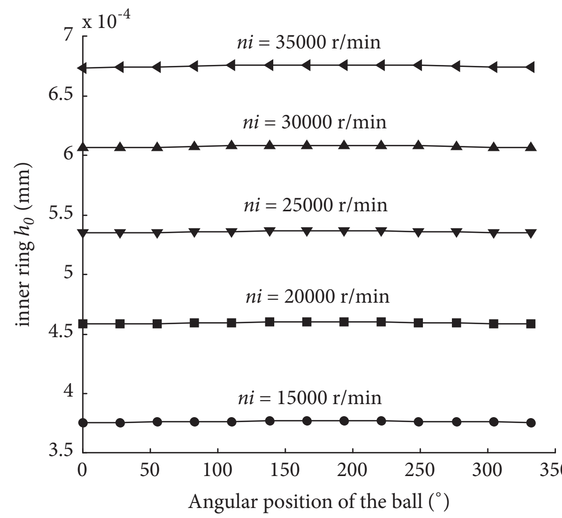

Figure 11: The influence of *ni* on oil film thickness between ball and inner ring.

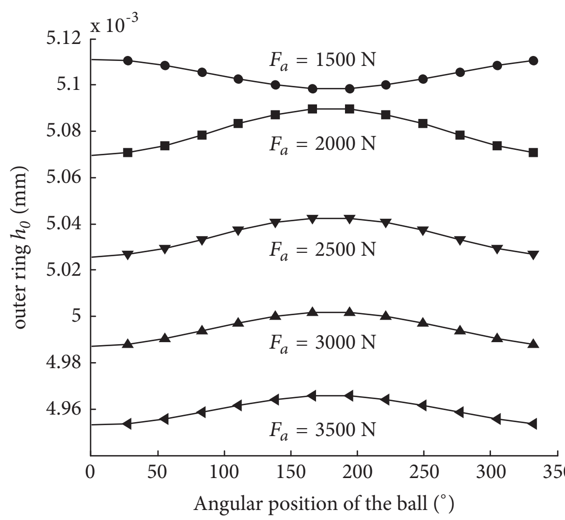

Figure 12: The influence of F_a on oil film thickness between ball and outer ring.

Figures 24–26 show that with the spindle speed of 30000 r/min and the thrust load of 3000 N, (i) the result values of dynamic characteristics of the contact load and bearing heat in MQSM are larger than that in TQSM when the radial load is beyond 1500 N, and (ii) the contact angle in MQSM is less than that in TQSM under the radial load of 2500 N. Therefore, the change of inner ring contact angle in MQSM is more stable than that in TQSM, which proves that the results of MQSM are more credible.

With the spindle speed of 30000 r/min and the axial load of 3000 N, Figures 27–29 show the dynamic characteristics with various RCR coefficients from 0.52 to 0.55 in MQSM and TQSM. Results indicate that all the values of the dynamic characteristics of the contact load, contact angle, and bearing heat in MQSM are less than those in TQSM. When RCR is more than 0.54, TQMS calculation results have a relatively

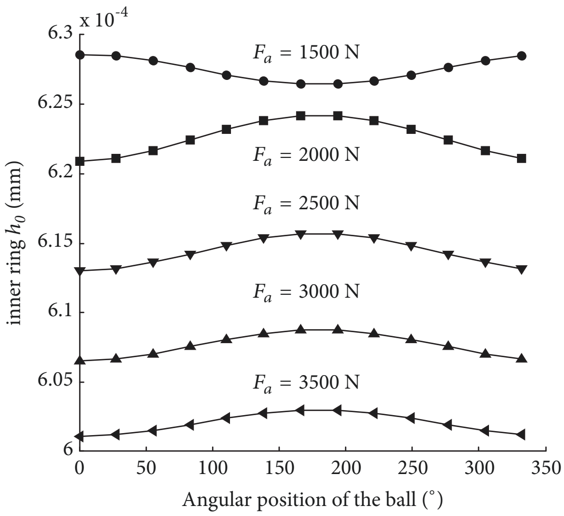

Figure 13: The influence of F_a on oil film thickness between ball and inner ring.

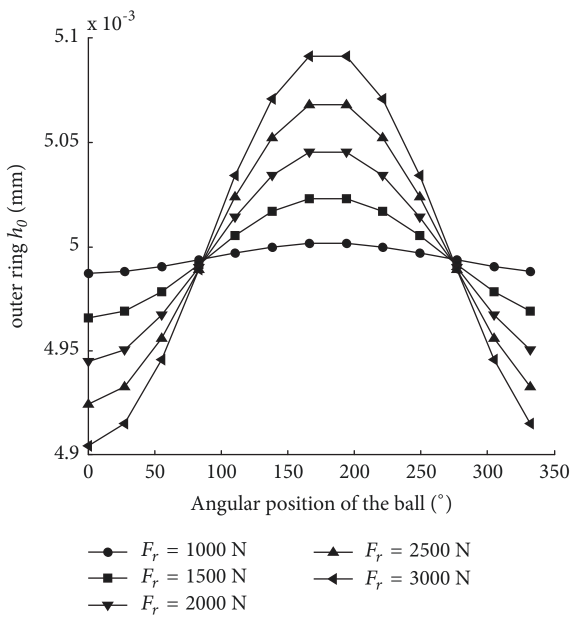

Figure 14: The influence of F_r on oil film thickness between ball and outer ring.

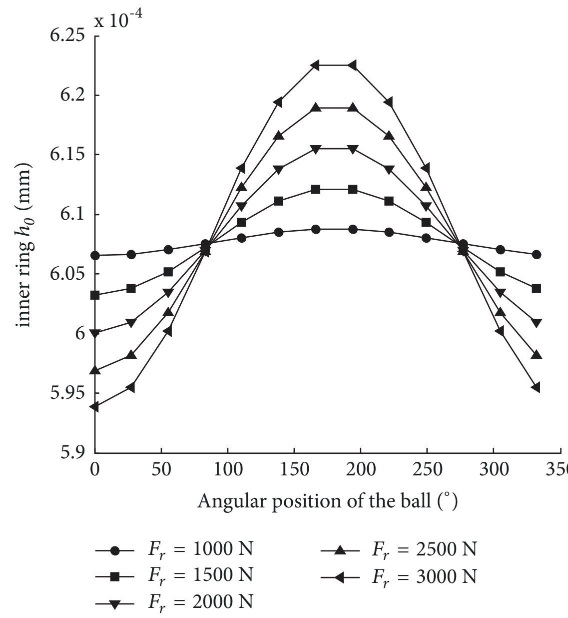

Figure 15: The influence of F_r on oil film thickness between ball and inner ring.

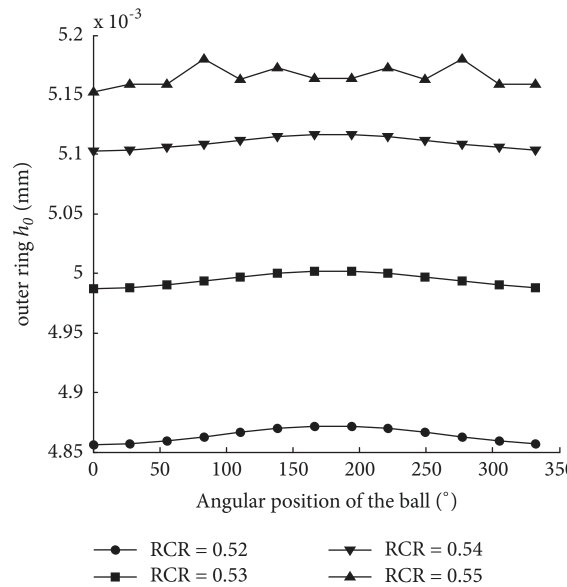

Figure 16: The influence of RCR on oil film thickness between ball and outer ring.

obvious mutation (except the inner ring contact angle). This is caused by the fact that the influence of oil film is not taken into account when calculating with TQMS. When RCR is greater than 0.54, the contact load and contact angle will increase, which will lead to the increase of heat generation. When calculating with MQMS, the lubricating oil film will form a layer of oil film between ball and raceway due to the consideration of lubrication, which will weaken the influence of the change of the curvature coefficient of the groove and will not cause mutation.

5.3. Conclusion. A modified quasi-statics model (MQSM) of spindle bearings was developed by introducing the oil film thickness and inner ring centrifugal deformation in this work. Experiments are conducted to evaluate the MQSM's results on the self-designed motorized spindle bearing rig. The dynamic characteristic values of the contact load, contact angle and bearing heat with various rotational speeds, axial loads, radial loads and RCR coefficients in MQSM are compared with those in TQSM. Results indicate that there are obvious differences of the dynamic characteristics under large radial load and RCR coefficients. Therefore, it can be concluded that the MQSM are more credible and accurate to

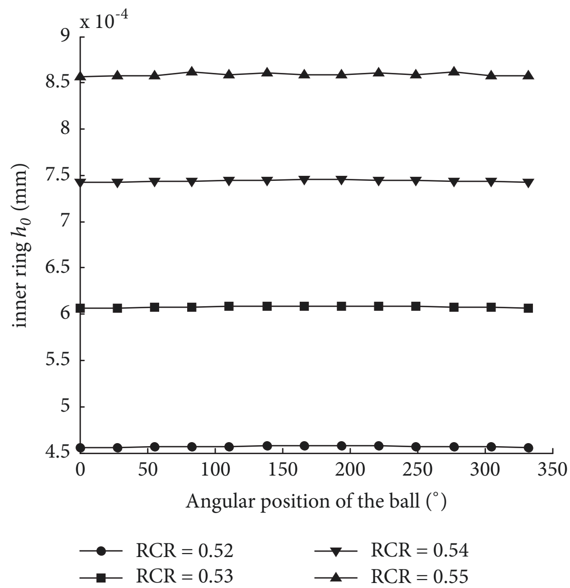

Figure 17: The influence of RCR on oil film thickness between ball and inner ring.

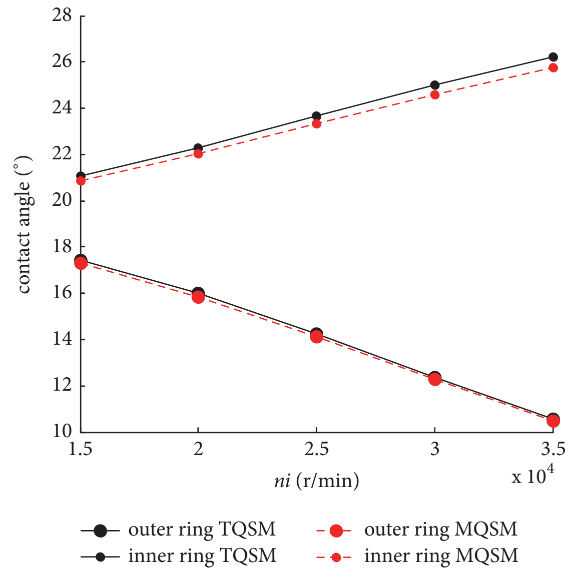

Figure 19: Contact angle with various *ni*.

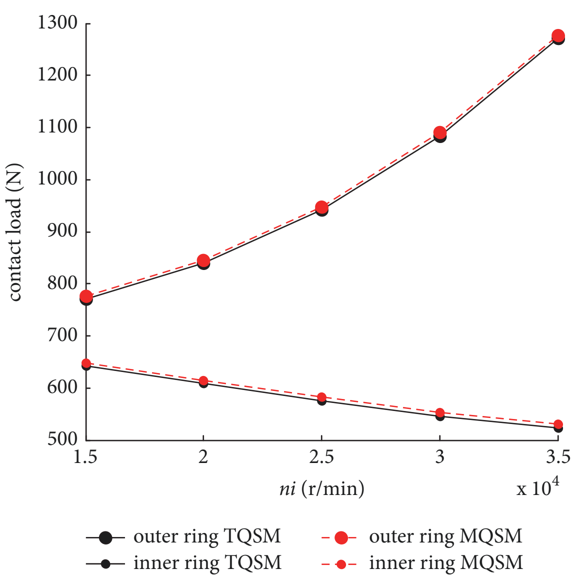

Figure 18: Contact load with various *ni*.

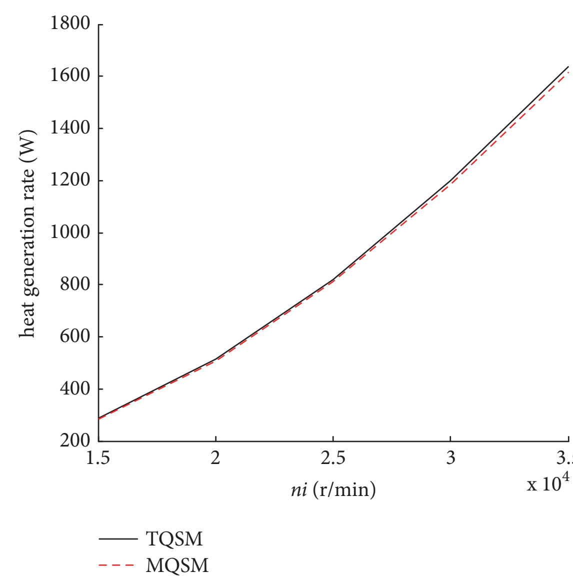

Figure 20: Heat generation rate with various *ni*.

be used to assess the spindle bearing dynamic characteristics. Future work will focus on the influence of various oil film thicknesses on the bearing dynamic characteristics.

Nomenclature

α: Semimajor axis of the contact area (mm)
A_a: Axial distances between the inner and outer channel curvature centers for the ball
A_r: Radial distances between the inner and outer channel curvature centers for the ball
C_D: Resistance coefficient
D_b: Ball diameter
D_b': Ball diameter after considering deformation
d_m: Bearing pitch diameter
d_i: Inner diameters
d_s: Inner diameter of the spindle
E_i: Elasticity modulus of inner ring
E_s: Elasticity modulus of shaft
f_i: Inner raceway groove curvature radius ratios
f_e: Outer raceway groove curvature radius ratios
F_c: Centrifugal force

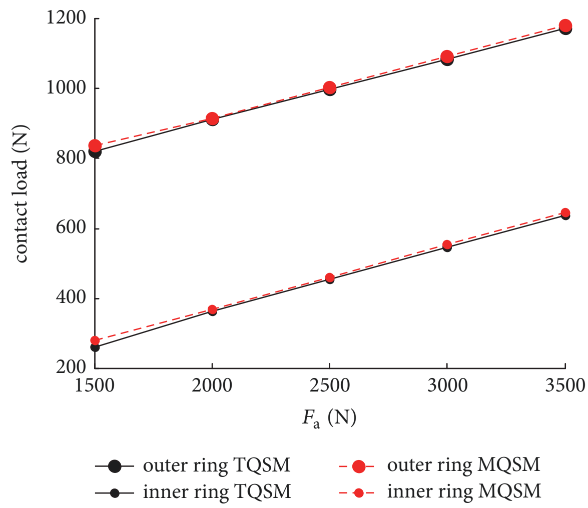

FIGURE 21: Contact load with various F_a.

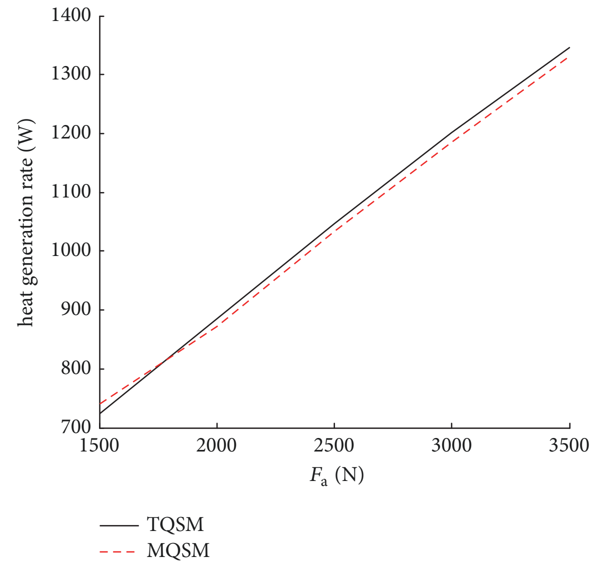

FIGURE 23: Heat generation rate with various F_a.

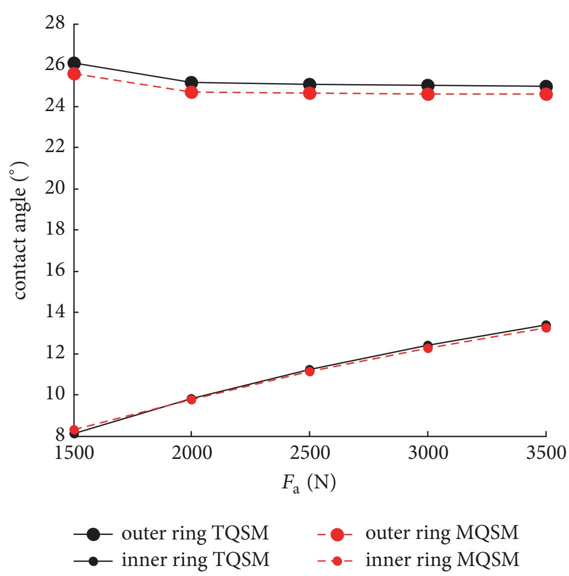

FIGURE 22: Contact angle with various F_a.

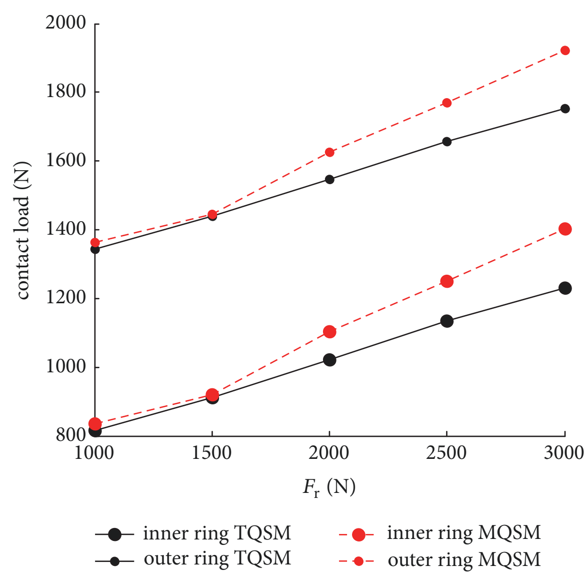

FIGURE 24: Contact load with various F_r.

F_r: Traction force
F_d: Resistance force
G : Dimensionless material parameters
h_0: Central oil film thickness
H_o: Dimensionless center oil film thickness
H_{min}: Dimensionless minimum oil film thickness
h: Center oil film thickness
Ic: Magnitude of interference caused by centrifugal expansion
J: Inertia moment
K: Stiffness coefficients
L: Distances between the ball center and the ring channel curvature centers
M_g: Gyroscopic moment
M_s: Spin torque
Q: Contact load
R_x: Equivalent r curvature radius of x
R_i: Circular radius of inner ring channel curvature center
U: Dimensionless velocity parameters
U_a: Axial changed distances of the center of channel curvature
V_r: Radial changed distances of the center of channel curvature
v_r: Relative sliding velocity
u_c: Centrifugal expansion deformation
W: Dimensionless load parameters
ω: Angular speed
ω_m: Orbital angular velocity
ω_b: Rotation angular velocity

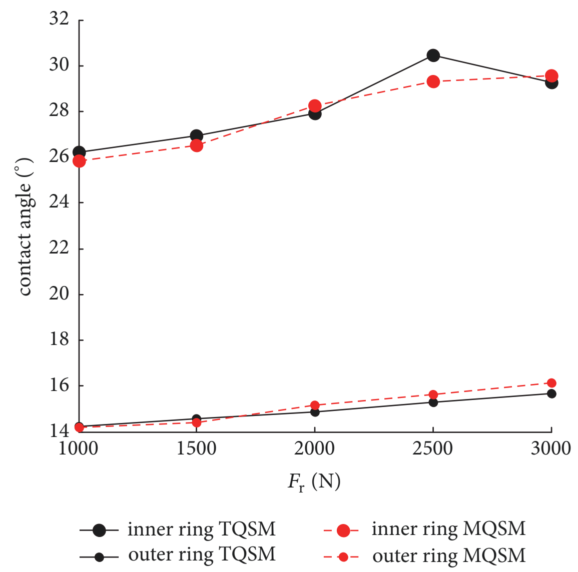

Figure 25: Contact angle with various F_r.

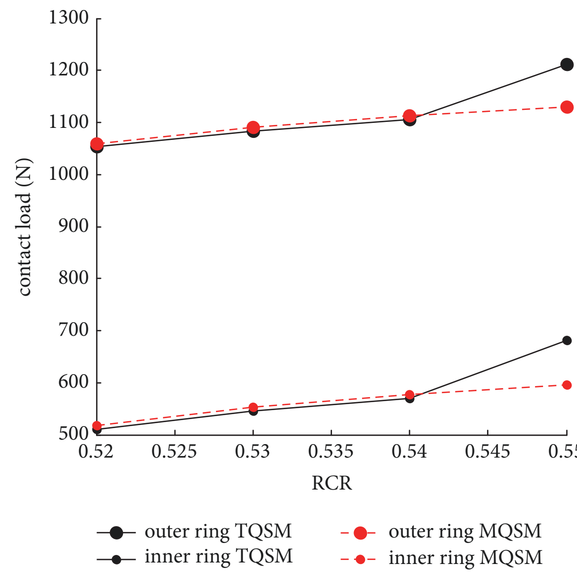

Figure 27: Contact load with various RCR.

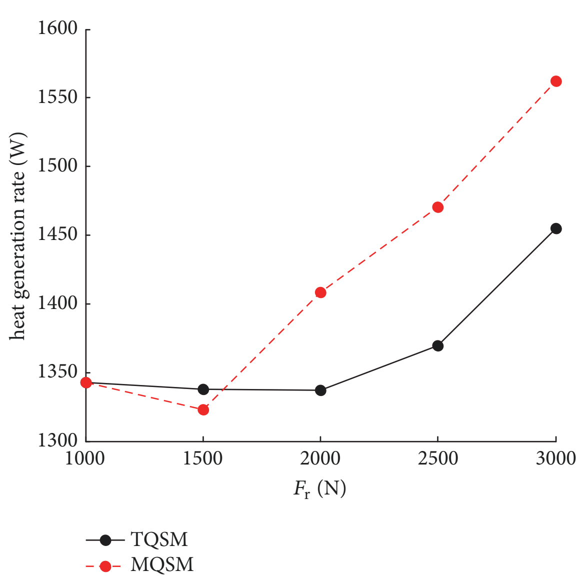

Figure 26: Heat generation rate with various F_r.

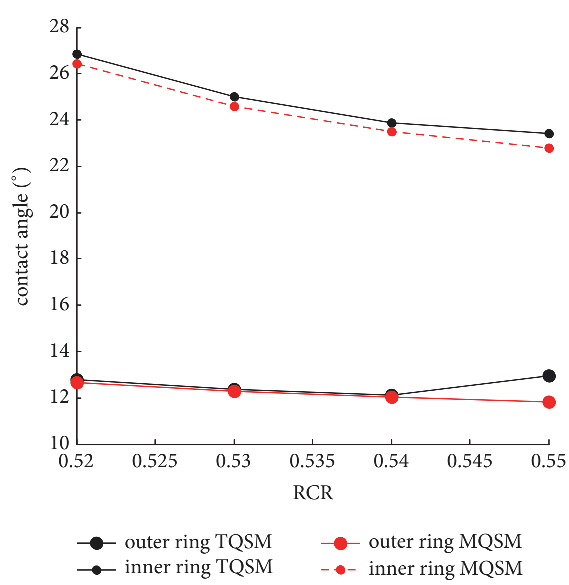

Figure 28: Contact angle with various RCR.

ω_s: Spin angular velocity
α: Contact angle
β: Spiral angle
β': Yaw angle
δ: Contact deformation
δ_a: Relative radial displacement
δ_r: Relative axial displacement
θ: Relative angular displacement
μ: Friction coefficient
Σ: Complete elliptic integral of the second kind
ρ: Density
ρ_{oa}: Density of the mixture gas
ν: Poison ratio
k: Ellipticity

Subscript

i : Inner ring
e: Outer ring
j: The jth ball
x, y, z: The ball coordinate components.

Data Availability

The data used to support the findings of this study are available from the corresponding author upon request.

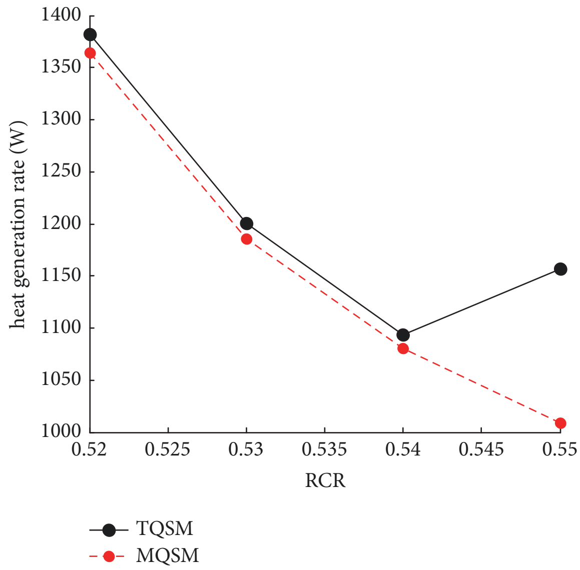

Figure 29: Heat generation rate with various RCR.

Conflicts of Interest

The authors confirm that there are no conflicts of interest.

Acknowledgments

This work was supported by the National Natural Science Foundation of China (No. 51805299), Shandong High School Research Project (J18KA004), and the subtopic of the program in the field of Intelligent Manufacturing and Advanced Materials, Scientific and Technological Innovation Plan (No. 13521103002) in Shanghai University.

References

[1] J. Wang, X. Du, Q. Hu, and S. Wang, “System design of spindle on high-precise CNC,” *Applied Mechanics and Materials*, vol. 151, pp. 463–468, 2012.

[2] Y. F. Yang, “The Study on Mechanical Reliability Design Method and Its Application,” in *Proceedings of the 2012 International Conference on Future Electrical Power And Energy System, Pt A*, J. Xiong, Ed., vol. 17, pp. 467–472, 2012.

[3] B. Wang, W. Sun, K. Xu, J. Zhang, and B. Wen, “The nonlinear stability prediction and fem modeling of high-speed spindle system with joints dynamic characteristics,” *Shock and Vibration*, vol. 2014, Article ID 153504, 12 pages, 2014.

[4] C.-W. Lin, Y.-K. Lin, and C.-H. Chu, “Dynamic models and design of spindle-bearing systems of machine tools: a review,” *International Journal of Precision Engineering and Manufacturing*, vol. 14, no. 3, pp. 513–521, 2013.

[5] D. Y. Tu, X. Wang, and A. H. Xu, “Virtual Design and Simulation for Biomass Plane-die Briquetting Machine,” in *Renewable And Sustainable Energy, Pts 1-7*, W. Pan, J. X. Ren, and Y. G. Li, Eds., vol. 347-353, pp. 2432–2437, 2012.

[6] J.-P. Hung, Y.-L. Lai, T.-L. Luo, and H.-C. Su, “Analysis of the machining stability of a milling machine considering the effect of machine frame structure and spindle bearings: experimental and finite element approaches,” *The International Journal of Advanced Manufacturing Technology*, vol. 68, no. 9–12, pp. 2393–2405, 2013.

[7] H. Cao, T. Holkup, X. Chen, and Z. He, “study of characteristic variations of high-speed spindles induced by centrifugal expansion deformations,” *Journal of Vibroengineering*, vol. 14, no. 3, pp. 1278–1291, 2012.

[8] B. Wang, W. Sun, K. P. Xu, and B. C. Wen, “Speed Effects on Inherent Rotating Frequency of Motorized Spindle System,” in *Mechatronics And Information Technology, Pts 1 And 2*, Q. Han, K. Takahashi, C. H. Oh, and Z. Luo, Eds., vol. 2-3, pp. 900–905, 2012.

[9] J. Hong, G. Liu, X. Li et al., “Influence of Bearing Configuration on Spindle Modal Characteristics,” in *Proceedings of the ASME 2014 International Mechanical Engineering Congress and Exposition*, Montreal, Quebec, Canada, 2015.

[10] W. Guo, H. Cao, Z. He, and L. Yang, “Fatigue Life Analysis of Rolling Bearings Based on Quasistatic Modeling,” *Shock and Vibration*, vol. 2015, Article ID 982350, 10 pages, 2015.

[11] S. Li, F. Yu, J. Shao, X. Huang, and B. Chen, “Study of dynamic characteristics about motorized spindle rotor-bearing system considering the effects of oil film stiffness,” in *Proceedings of the The 2015 International Conference on Design, Manufacturing and Mechatronics (ICDMM2015)*, pp. 1354–1366, Wuhan, China, 2016.

[12] D. Chen, S. Zhou, L. Dong, and J. Fan, “Performance evaluation and comparative analysis of hydrostatic spindle affect by the oil film slip,” *Journal of Manufacturing Processes*, vol. 20, pp. 128–136, 2015.

[13] D. J. Chen, Y. H. Bian, J. W. Fan, and F. H. Zhang, “Performance of Hydrostatics Spindle Under Effect of Mass Unbalance,” in *Mechanical Design And Power Engineering, Pts 1 And 2*, A. S. Babu, Ed., vol. 490-491, pp. 910–913, 2014.

[14] F. Jiao, G. M. Sun, and J. H. Liu, “Research on the Dynamic Characteristics of NC Boring Machine Spindle System Based on Finite Element Analysis,” in *Contemporary Design And Manufacturing Technology*, T. Wang, H. Guo, D. Zuo, and J. Xu, Eds., vol. 819, pp. 71–75, 2013.

[15] D. Lu, K. Liu, W. Zhao, and B. Lu, “Thermal Characteristics of Water-Lubricated Ceramic Hydrostatic Hydrodynamic Hybrid Bearings,” *Tribology Letters*, vol. 63, no. 2, 2016.

[16] L. Wu and Q. Tan, “A study of cooling system in a grease-lubricated precision spindle,” *Advances in Mechanical Engineering*, vol. 8, no. 8, 2016.

[17] X. H. Li, H. F. Li, J. Hong, and Y. F. Zhang, “Heat analysis of ball bearing under nonuniform preload based on five degrees of freedom quasi-static mode,” *Proceedings of the Institution of Mechanical Engineers, Part J: Journal of Engineering Tribology*, 2016.

[18] S.-W. Kim, K. Kang, K. Yoon, and D.-H. Choi, “Design optimization of an angular contact ball bearing for the main shaft of a grinder,” *Mechanism and Machine Theory*, vol. 104, pp. 287–302, 2016.

[19] S. Kabus, M. R. Hansen, and O. Ø. Mouritsen, “A new quasi-static multi-degree of freedom tapered roller bearing model to accurately consider non-Hertzian contact pressures in time-domain simulations,” *Proceedings of the Institution of Mechanical Engineers, Part K: Journal of Multi-body Dynamics*, vol. 228, no. 2, pp. 111–125, 2014.